Pressure-induced topological insulator-to-metal transition and superconductivity in Sn-doped $Bi_{1.1}Sb_{0.9}Te_2S$

Chao An,[1,2] Xuliang Chen,[1,*] Bin Wu,[3] Yonghui Zhou,[1] Ying Zhou,[1] Ranran Zhang,[1]
Changyong Park,[4] Fengqi Song,[3,5] and Zhaorong Yang[1,5,6,†]

[1]*Anhui Province Key Laboratory of Condensed Matter Physics at Extreme Conditions, High Magnetic Field Laboratory,*
Chinese Academy of Sciences, Hefei 230031, China
[2]*University of Science and Technology of China, Hefei 230026, China*
[3]*National Laboratory of Solid State Microstructures, School of Physics, Nanjing University, Nanjing 210093, China*
[4]*HPCAT, Geophysical Laboratory, Carnegie Institution of Washington, Argonne, Illinois 60439, USA*
[5]*Collaborative Innovation Center of Advanced Microstructures, Nanjing 210093, China*
[6]*Institute of Physical Science and Information Technology, Anhui University, Hefei 230601, China*

Tetradymite-type topological insulator Sn-doped $Bi_{1.1}Sb_{0.9}Te_2S$ (Sn-BSTS), with a surface state Dirac point energy well isolated from the bulk valence and conduction bands, is an ideal platform for studying the topological transport phenomena. Here, we present high-pressure transport studies on single-crystal Sn-BSTS, combined with Raman scattering and synchrotron x-ray diffraction measurements. Over the studied pressure range of 0.7–37.2 GPa, three critical pressure points can be observed: (i) At $\sim$9 GPa, a pressure-induced topological insulator-to-metal transition is revealed due to closure of the bulk band gap, which is accompanied by changes in slope of the Raman frequencies and a minimum in c/a within the pristine rhombohedral structure (R-$3m$); (ii) at $\sim$13 GPa, superconductivity is observed to emerge, along with the R-$3m$ to a $C2/c$ (monoclinic) structural transition; (iii) at $\sim$24 GPa, the superconducting transition onset temperature T_C reaches a maximum of $\sim$12 K, accompanied by a second structural transition from the $C2/c$ to a body-centered cubic Im-$3m$ phase.

I. INTRODUCTION

Pressure tuning of structural and electrical properties in tetradymite-type topological insulators (TIs) like Bi_2Se_3, Bi_2Te_3, and Sb_2Te_3 has attracted much attention because of discoveries of a variety of interesting phenomena [1–22]. For instance, synchrotron x-ray diffraction and Raman scattering measurements in Bi_2Se_3 reveal a minimum in the lattice parameters ratio c/a and changes in pressure dependences of the Raman frequencies at the same low pressure far before a structural phase transition [1]; meanwhile, discontinuities in conductivity are observed around this critical pressure [2]. Similar situations are also encountered in other members of tetradymite-type TIs [3–10], despite the critical pressures being somewhat different. Due to the absence of a structural transition, these anomalies were usually related to a pressure-induced electronic topological transition (ETT) or Lifshitz transition. As is known, the Lifshitz transition [23] links to the van Hove singularity associated with the band extrema passing through the Fermi level, and in the presence of such transition the distribution of carriers and Fermi surface topology changes. Considering the lack of such changes, Bera *et al.* [11] thus termed the transition as an isostructural transition, instead of the ETT. Obviously, the origins of these anomalies still remain elusive. Besides,

superconductivity is commonly observed in these TIs at high pressures [12–17]. Interest is widely sparked by the expectation of realizing topological superconductivity [16], in spite of the absence of direct experimental evidence so far.

TI is characterized by the insulating bulk state and metallic topological surface states (TSSs) that are protected by time-reversal symmetry. Ideally, a surface state Dirac point energy is isolated well from the bulk valence and conduction bands. Experimentally, for as-grown tetradymite-type nominally stoichiometric TIs, a metallic bulk conduction arising from inherent Se/Te deficiencies usually overwhelms the surface transport [24–26]. Therefore, it is hard to unveil the pressure evolutions of the intrinsic conductions of the bulk insulating state and TSSs via transport, which in turn may result in misunderstanding of the structural responses to external pressure.

In view of the above, here we present a systematic study of the electrical, structural, and vibrational properties on a recently discovered TI Sn-doped $Bi_{1.1}Sb_{0.9}Te_2S$ (Sn-BSTS) [27] in diamond anvil cells with pressures up to 37.2 GPa, which has a well-isolated bulk state from the TSSs. Thanks to the unique band structure of Sn-BSTS, we can successfully trace the pressure evolutions of the bulk and TSSs conductivities separately, which are vital for unveiling the topological insulator-to-metal transition–related structural and vibrational anomalies, instead of an ETT. Interestingly, the T_C maximum of $\sim$12 K obtained here is the highest value among all the pressurized tetradymite-type TIs.

*xlchen@hmfl.ac.cn
†zryang@issp.ac.cn

II. EXPERIMENTAL DETAILS

Sn-BSTS single crystals were grown by a modified Bridgman technique [28]. The high quality of the single crystals was checked by single-crystal and powder x-ray diffractions as well as energy dispersive spectra (see Fig. S1 and notes in the Supplemental Material for more details [29]). A standard four-probe method was employed to perform the high-pressure electrical transport measurements in a temperature range of 1.8–300 K in a Be-Cu diamond anvil cell (DAC), designed by the Honest Machinery Designer's office (HMD), Japan. A piece of single crystal cleaved from the bulk Sn-BSTS single crystal was loaded with sodium chloride (NaCl) powder as the pressure transmitting medium and the current were introduced in the *ab* plane.

Pressure was generated by a Mao-Bell–type symmetric DAC for the synchrotron x-ray diffraction (XRD) and Raman scattering measurements. Raman scattering measurements were performed at room temperature on freshly cleaved Sn-BSTS single crystals using 532-nm solid-state laser for excitation with the power below 1% to avoid sample damage

and any heating effect, at the Center for High Pressure Science and Technology Advanced Research (HPSTAR) in Shanghai. Neon was used as the pressure transmitting medium. We also repeated our high-pressure Raman measurements at the China High Magnetic Field Laboratory (CHMFL) in Hefei using Daphne 7373 as the pressure medium. High-pressure synchrotron powder XRD ($\lambda = 0.4133$ Å) was performed at room temperature at the beamline of 16 BM-D, HPCAT [30] of the Advanced Photon Source, Argonne National Laboratory. Daphne 7373 was used as the pressure transmitting medium. The DIOPTAS [31] program was used for image integrations and the Le Bail method was employed to fit the XRD data with the RIETICA [32] program. The ruby fluorescence method [33] was used to determine the pressure for all of the above experiments.

III. RESULTS AND DISCUSSION

Figure 1(a) displays the temperature (T) dependence of the electrical resistance (R) of the Sn-BSTS single crystal at pressures from 0.7 to 10.5 GPa. At 0.7 GPa, a huge
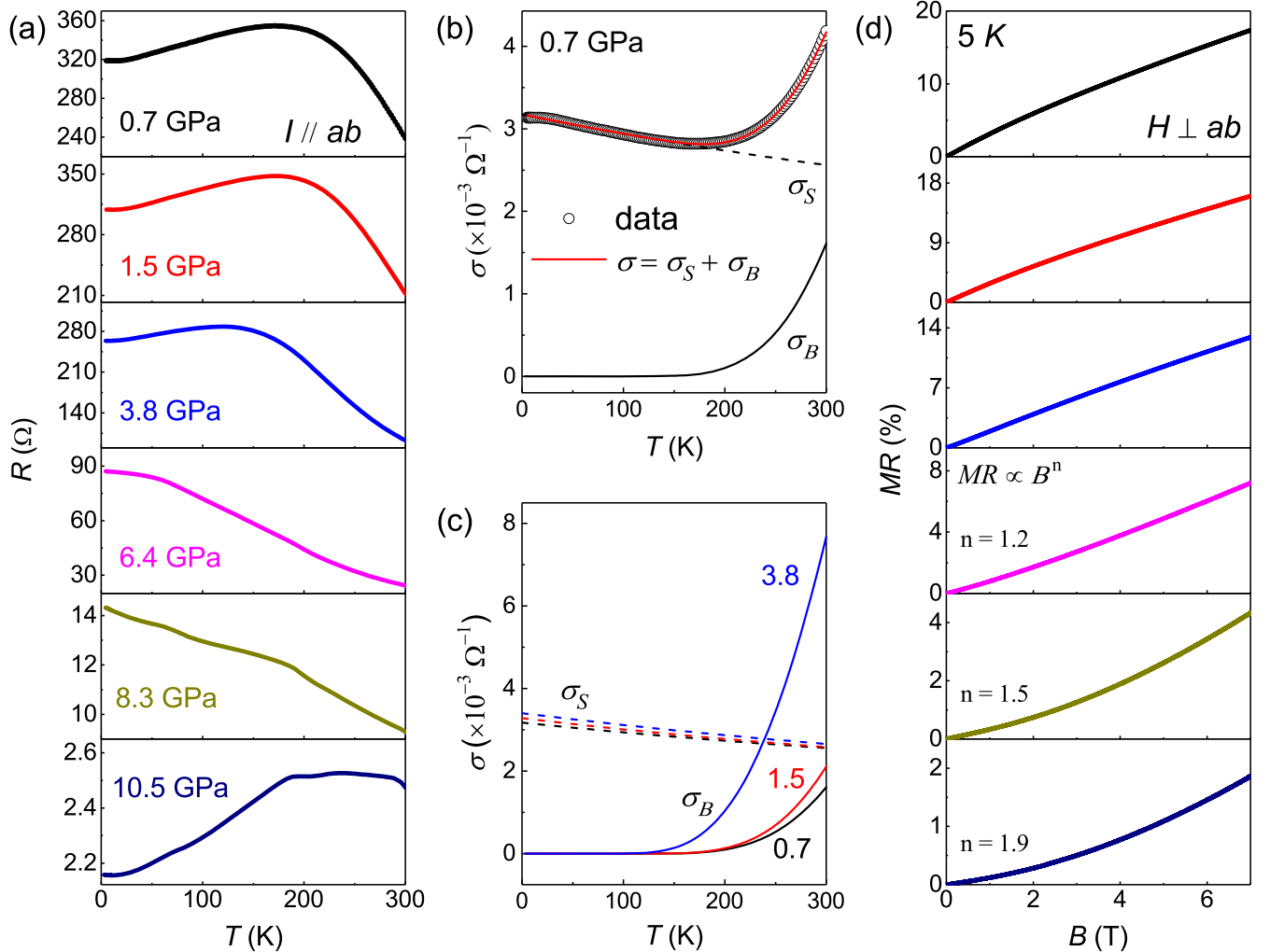

FIG. 1. (a) Resistance (R) versus temperature (T) curves in the pressure range of 0.7–10.5 GPa. The current (I) is introduced in the *ab* plane of the single crystal. (b) Temperature dependence of the conductivity at 0.7 GPa fitted by the formula of $\sigma(T) = \sigma_S(T) + \sigma_B(T)$ (red line). More details can be found in the main text. (c) Evolutions of the surface and bulk conductivities with pressures to 3.8 GPa. (d) Magnetoresistance (MR) measured at 5 K and 7 T under pressures to 10.5 GPa.

resistance hump at $T_h \sim 170$ K is observed, in agreement with that measured at ambient pressure [27]. At ambient pressure, the conductance of Sn-BSTS is considered as a sum of two parallel channels: surface (σ_S) and bulk (σ_B) conductances [34]. For simplicity, a two-channel model with the formula of $\sigma(T) = \sigma_S(T) + \sigma_B(T)$ is employed. The former contribution is written as $\sigma_S(T) = 1/\rho_S(T)$, where $\rho_S(T) = \rho_0 + bT^2 + cT$, while the latter one is expressed as $\sigma_B(T) = 1/\rho_B(T)$, where $\rho_B(T) = a\exp(E_g/2k_BT)$ [35]. Figure 1(b) shows the fitting results with the two-channel model at 0.7 GPa, in which the dashed and solid lines represent σ_S and σ_B, respectively. It yields a bulk band gap $E_g = 294$ meV, which is a little smaller than 350 meV revealed by ARPES for Sn-BSTS at ambient pressure [27]. Upon compression to 3.8 GPa, the T_h shifts towards lower temperatures rapidly, which indicates that the contribution of the bulk state to the total conductivity becomes increasingly dominant. As displayed in Fig. 1(c), the conductivity of the bulk state shows a rapid enhancement with increasing pressure, while that of the surface state increases marginally upon compression. At 6.4 GPa, the resistance exhibits a semiconductinglike behavior in the whole temperature range, suggesting that the contribution of topological surface states (TSSs) are overwhelmed by that of the bulk state. Further increasing the pressure to 10.5 GPa, a partial metallic behavior below 190 K is observed, signaling the metallization of the bulk state.

As the contribution of the TSSs can also be identified through magnetotransport measurements, magnetoresistance (MR) was measured at 5 K under various pressures up to 10.5 GPa with magnetic fields perpendicular to the ab plane, as shown in Fig. 1(d). One can see that the MR decreases monotonically with increasing pressure. In the low-pressure region of 0.7–3.8 GPa, MR exhibits a concave behavior, which is very similar to that observed in the tetradymite-type TIs and can be attributed to weak antilocalization originating from the TSSs [36,37]. Further increasing the pressure, the MR changes to a convex behavior at 6.4 GPa, above which a classical power-law behavior ($MR \propto H^2$) develops gradually. These observations indicate that the bulk state conductance dominates above 6.4 GPa, in excellent consistence with the results from the R-T data shown in Fig. 1(a).

Upon further compression to 12.6 GPa, a pronounced resistance drop is clearly seen below ~ 4 K as presented in Figs. 2(a) and 2(b). Zero resistance is observed at 14.3 GPa, suggesting the appearance of superconductivity in the pressurized Sn-BSTS. The presence of superconductivity is further confirmed by the temperature dependence of resistance measurements under various magnetic fields perpendicular to the ab plane at 14.3 GPa. As shown in Fig. 2(c), the superconducting transition temperature T_C is monotonically decreased with increasing magnetic field and the resistance drop is almost smeared out at 1.5 T. The inset of Fig. 2(c) shows the upper critical field $\mu_0 H_{C2}$ as a function of temperature. Here the $\mu_0 H_{C2}$ value is defined from the resistance criterion of $R_{cri} = 90\% R_n$ (R_n is the normal state resistance near T_C). The upper critical field $\mu_0 H_{C2}$ is estimated to be 2.31 T according to the Werthamer-Helfand-Hohenberg (WHH) equation [38].

To check the relationship between superconductivity and structure, *in situ* high-pressure synchrotron XRD measurements were performed on powdered single-crystal Sn-BSTS up to 31.6 GPa. The experimental patterns are presented in Fig. 3(a). Upon compression, the rhombohedral structure (R-$3m$) of Sn-BSTS is found to be stable up to 11.7 GPa, above which several new peaks show up as denoted by
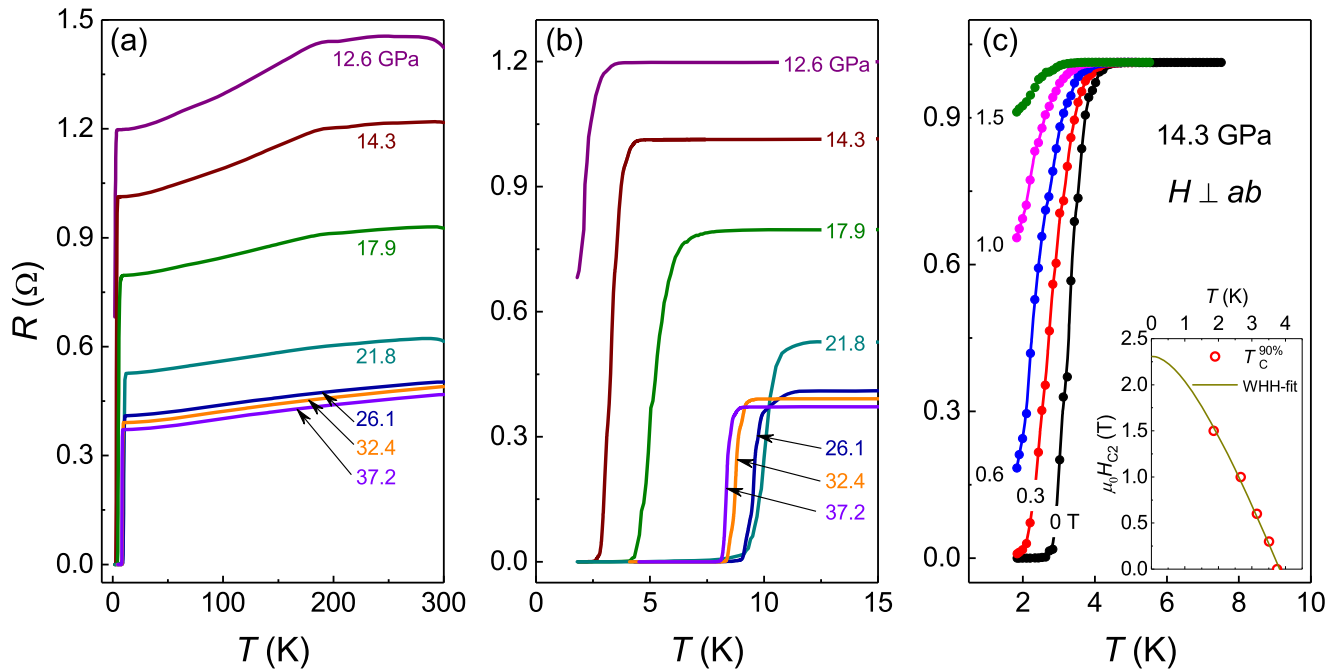

FIG. 2. (a) Temperature dependence of the resistance in the pressure range of 12.6–37.2 GPa. (b) An enlarged view of the low-temperature resistance, highlighting the superconducting transition. (c) Temperature dependence of the resistance under different magnetic fields up to 1.5 T. The applied pressure is 14.3 GPa. Inset of (c) shows temperature dependence of the upper critical field $\mu_0 H_{C2}$ (T). The solid line is the WHH fit to the data and $\mu_0 H_{C2}(0)$ is estimated to be 2.31 T.
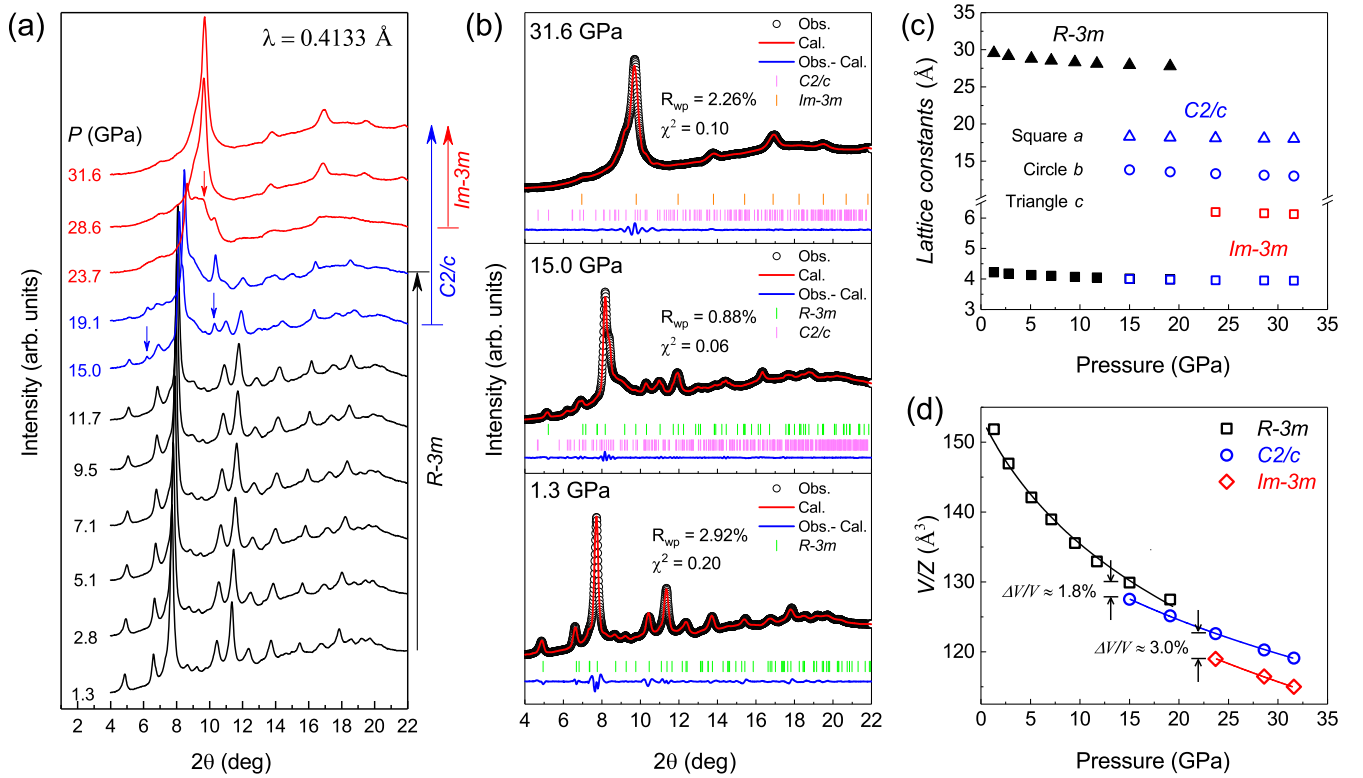
FIG. 3. (a) Synchrotron x-ray diffraction patterns of Sn-BSTS at room temperature with pressures up to 31.6 GPa ($\lambda = 0.4133\,\text{Å}$). (b) Typical Rietveld refinement results at 1.3, 15.0, and 31.6 GPa by using the Le Bail method. (c) Lattice parameters as a function of pressure. (d) The unit-cell volume versus pressure. The data were fitted by the third-order Birch-Murnaghan formula.

arrows, suggesting occurrence of a structural transition. In the intermediate pressure range, this new structural phase is observed to coexist with the low-pressure pristine one. With increasing pressure above 19.1 GPa, the low-pressure $R\text{-}3m$ phase disappears completely, while another new structural phase transition takes place, as indicated by appearance of new peaks. Both high-pressure phases coexist up to the highest pressure of 31.6 GPa achieved in the present study. We also plot the phase quantification as a function of pressure in Fig. S2 (Supplemental Material [29]). In addition to two critical pressures relating to the structural phase transition, phase coexistences and their respective evolutions with pressure are also clearly revealed. After carefully analyzing and fitting the data, we found that the pressure-induced structural transition sequence in Sn-BSTS is $R\text{-}3m \rightarrow C2/c \rightarrow Im\text{-}3m$, in agreement with those observed in its brother compounds Bi_2Te_3 and Sb_2Te_3 [18–20]. Typical standard Rietveld refinements at 1.3, 15.0, and 31.6 GPa are displayed in Fig. 3(b). The corresponding fit parameters are displayed in Table S1 [29].

The detailed lattice parameters and volume as a function of pressure are exhibited in Figs. 3(c) and 3(d). The equation of state (EOS) was fitted by using the third-order Birch-Murnaghan formula [39]:

$$P = \frac{3}{2}B_0[(V_0/V)^{7/3} - (V_0/V)^{5/3}]$$
$$\times \left\{1 + \frac{3}{4}(B'_0 - 4)[(V_0/V)^{2/3} - 1]\right\}, \quad (1)$$

where V_0, B_0, and B'_0 are the volume, bulk modulus $-V/(dV/dP)$, and first-order derivative of the bulk modulus at

zero pressure, respectively. The fitting yields $V_0 = 153.7\,\text{Å}^3$, $B_0 = 51.4\,\text{GPa}$, and $B'_0 = 7.0$ for the $R\text{-}3m$ phase; $141.7\,\text{Å}^3$, $97.2\,\text{GPa}$, and 7.4 for the $C2/c$ phase; and $137.5\,\text{Å}^3$, $122.9\,\text{GPa}$, and 4.0 for the $Im\text{-}3m$ phase. In addition, the volume collapses at these two structural transition pressures are estimated to be about 1.8% and 3.0%, respectively, indicating both structural transitions are first order.

The structural transitions are also reflected in Raman measurements as shown in Fig. 4. At 1.3 GPa, two main peaks centered at 112.7 and 170.4 cm^{-1} are observed, similar to those observed at ambient pressure (Fig. S1(d) [29] and Ref. [27]). These two peaks can be assigned to the E_g and A_{2g} vibrational modes [27], respectively. With increasing pressure, both Raman peaks move towards higher frequencies monotonically. At 12.6 GPa, a new peak at 156.8 cm^{-1} develops due to the structural transition from $R\text{-}3m$ to $C2/c$, which can be assigned to the A_g mode [4,6]. Upon further compression above 24.2 GPa, all Raman mode disappears relating to the structural transition from $C2/c$ to $Im\text{-}3m$. These conclusions are reproducible from a second high-pressure Raman experiment except for a minor difference in the critical pressure values (Fig. S3 [29]).

To obtain a comprehensive understanding of the pressure-induced metallization and superconductivity in TI Sn-BSTS, the pressure dependences of the frequency and full width at half maximum (FWHM) of Raman modes, lattice parameters ratio c/a, bulk gap E_g, and superconducting critical temperature T_C are plotted together in Fig. 5. It is found that the lattice ratio c/a shows a minimum around 9 GPa [Fig. 5(a)]. Concurrently, clear
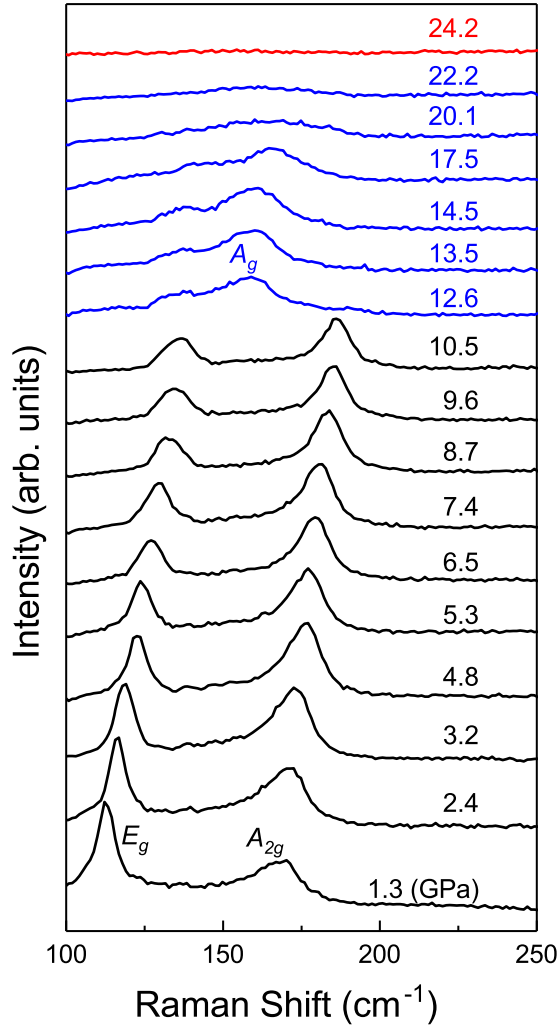
FIG. 4. Selected Raman spectra of Sn-BSTS at room temperature with pressures up to 24.2 GPa.
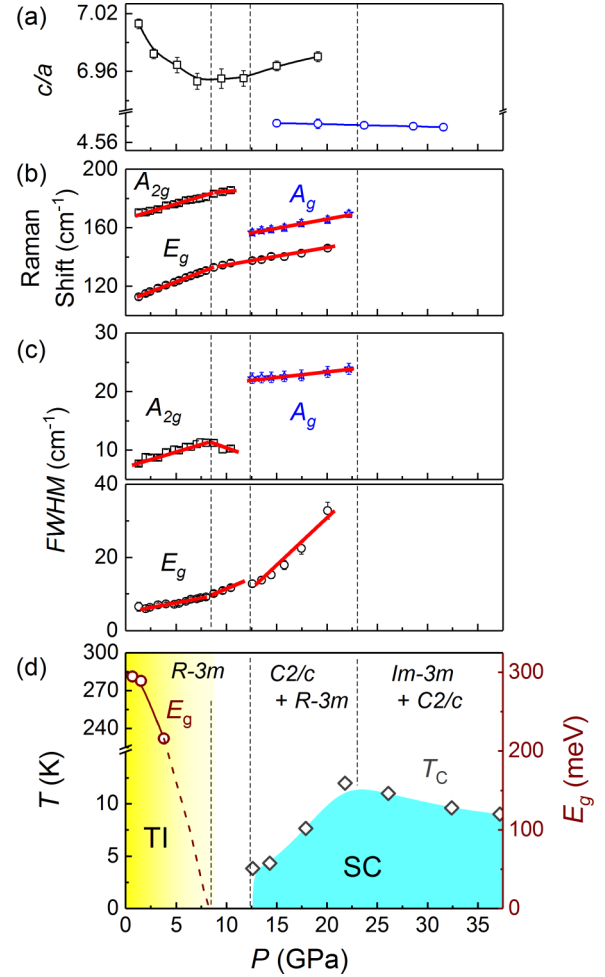

FIG. 5. (a) Lattice ratio of c/a as a function of pressure. (b) Pressure dependence of Raman frequencies of Sn-BSTS. Solid lines are linear fits to data. (c) Pressure dependence of FWHM of Sn-BSTS. Solid line denotes linear fits to data. (d) Pressure-temperature diagram of Sn-BSTS. The left axis stands for temperature T and the right axis corresponds to the bulk band gap E_g. "TI" and "SC" denote topological insulators and superconductivity, respectively.

changes in the slope of Raman frequencies and the FWHM of the E_g and A_{2g} mode are observed [Figs. 5(b) and 5(c)]. Meanwhile, closure of the bulk gap is estimated at ~9 GPa by extrapolating the E_g versus P curve [wine dashed line in Fig. 5(d)]. Consequently, all of these structural and vibrational anomalies at ~9 GPa should be related to the closure of the bulk gap, i.e., a pressure-induced topological insulator-to-metal transition, through electron-phonon coupling [40,41].

We note that similar anomalous behaviors have been reported in previous high-pressure studies of tetradymite-type TIs, which were attributed to an electronic topological transition (ETT) [1,4–9]. On the one hand, to check whether there is an ETT in Sn-BSTS or not, we have plotted the reduced pressure versus Eulerian strain [5]. In Fig. S4 [29], one can see that only linear behaviors are observed, in stark contrast to previous cases, probably indicating the absence of ETT. On the other hand, as reported previously, the transport behavior in these parent TIs is dominated by the inherent impurity states [24,26]. The impurity states contribute a metallic transport that overwhelms the contributions from the TSSs, resulting in the experimentally observed metallic feature in R-T [24]. Therefore, the interference from the impurity states may

mask the pressure effect on inherent electrical, structural, and vibrational responses of both TSSs and bulk state. In the present case, due to the unique electrical band structure of TI Sn-BSTS, we can trace the pressure dependencies of the TSSs and bulk state separately. Importantly, a pressure-induced topological insulator-to-metal transition of Sn-BSTS is successfully unveiled, which is simultaneously accompanied by structural and vibrational anomalies. In view of the above two points, we argue that the previously observed anomalies in pressurized tetradymite-type parent TIs might be related to the closure of the bulk band gap of the topological insulator, instead of the ETT [1,4–7].

Upon further increasing pressure, another two critical pressures can be clearly discerned relating to the successive structural transitions. Accompanied by the first structural transition, superconductivity is observed at ~13 GPa with T_C ~ 3.8 K. Further increasing the pressure, the FWHM of the A_g mode is observed to enhance gradually, implying an increasing electron-phonon coupling [40,41]. Meanwhile,

T_C also increases rapidly [Fig. 5(d)], probably hinting at a phonon-mediated superconductivity. T_C reaches a maximum value of $\sim$12 K at 21.8 GPa, around which the second structural transition happens.

In the tetradymite-type TIs family [12,15–17,42], the occurrence of superconductivity under high pressure is commonly accompanied by a structural transition or structural instability; the T_C increases rapidly and reaches a maximum at a higher pressure, where a second structural transition appears. This is also true for the present case of Sn-BSTS. However, the T_C trend in the second high-pressure structural phase is somewhat different. In the Se-dominated compounds, for example, Bi_2Se_3 [15] and $Sr_{0.065}Bi_2Se_3$ [42], T_C stays almost constant with pressure, which was considered as an indication of unconventional superconductivity; in Te-dominated compounds, for example, Bi_2Te_3 [12] and here Sn-BSTS, T_C decreases gradually with pressure. This might be related to a difference in the high-pressure structural symmetries: Generally a tetragonal $I4/mmm$ or a bcc-like $C2/m$ lattice develops for the former while a cubic Im-$3m$ lattice develops for the latter. Interestingly, the T_C maximum obtained here is the highest value in this TIs family studied so far.

IV. CONCLUSIONS

In summary, we have investigated the high-pressure electrical, structural, and vibrational properties of TI Sn-doped $Bi_{1.1}Sb_{0.9}Te_2S$ with pressures up to 37.2 GPa. With increasing pressure, a pressure-induced metallization from closure of the bulk gap is revealed around 9 GPa, accompanied by a change

in slope of the Raman modes and a minimum in the lattice ratio of c/a. Furthermore, superconductivity is observed at 12.6 GPa and T_C reaches the maximum of $\sim$12 K at 21.8 GPa, which is the highest T_C ever reported in tetradymite-type TIs. Based on the synchrotron XRD and Raman measurements, the appearance of superconductivity and the decrease in T_C could be related to successive structural transitions.

[1] R. Vilaplana, D. Santamaría-Pérez, O. Gomis, F. J. Manjón, J. González, A. Segura, A. Muñoz, P. Rodríguez-Hernández, E. Pérez-González, V. Marín-Borrás, V. Muñoz-Sanjose, C. Drasar, and V. Kucek, Phys. Rev. B **84**, 184110 (2011).

[2] J. K. Zhang, Y. H. Han, C. L. Liu, X. Zhang, F. Ke, G. Peng, Y. M. Ma, Y. Z. Ma, and C. X. Gao, Appl. Phys. Lett. **105**, 062102 (2014).

[3] A. Nakayama, M. Einaga, Y. Tanabe, S. Nakano, F. Ishikawa, and Y. Yamada, High Pressure Res. **29**, 245 (2009).

[4] O. Gomis, R. Vilaplana, F. J. Manjón, P. Rodríguez-Hernández, E. Pérez-González, A. Muñoz, V. Kucek, and C. Drasar, Phys. Rev. B **84**, 174305 (2011).

[5] A. Polian, M. Gauthier, S. M. Souza, D. M. Trichês, J. Cardoso de Lima, and T. A. Grandi, Phys. Rev. B **83**, 113106 (2011).

[6] R. Vilaplana, O. Gomis, F. J. Manjón, A. Segura, E. Pérez-González, P. Rodríguez-Hernández, A. Muñoz, J. González, V. Marín-Borrás, V. Muñoz-Sanjosé, C. Drasar, and V. Kucek, Phys. Rev. B **84**, 104112 (2011).

[7] G. K. Pradhan, A. Bera, P. Kumar, D. V. S. Muthu, and A. K. Sood, Solid State Commun. **152**, 284 (2012).

[8] S. M. Souza, C. M. Poffo, D. M. Trichês, J. C. de Lima, T. A. Grandi, A. Polian, and M. Gauthier, Phys. B (Amsterdam, Neth.) **407**, 3781 (2012).

[9] F. J. Manjón, R. Vilaplana, O. Gomis, E. Pérez-González, D. Santamaría-Pérez, V. Marín-Borrás, A. Segura, J. González, P. Rodríguez-Hernández, A. Muñoz, C. Drasar, V. Kucek, and V. Muñoz-Sanjosé, Phys. Status Solidi B **250**, 669 (2013).

[10] J. K. Zhang, C. L. Liu, X. Zhang, F. Ke, Y. H. Han, G. Peng, Y. Z. Ma, and C. X. Gao, Appl. Phys. Lett. **103**, 052102 (2013).

[11] A. Bera, K. Pal, D. V. S. Muthu, U. V. Waghmare, and A. K. Sood, J. Phys.: Condens. Matter **28**, 105401 (2016).

[12] K. Matsubayashi, T. Terai, J. S. Zhou, and Y. Uwatoko, Phys. Rev. B **90**, 125126 (2014).

[13] J. Zhu, J. L. Zhang, P. P. Kong, S. J. Zhang, X. H. Yu, J. L. Zhu, Q. Q. Liu, X. Li, R. C. Yu, R. Ahuja, W. G. Yang, G. Y. Shen, H. K. Mao, H. M. Weng, X. Dai, Z. Fang, Y. S. Zhao, and C. Q. Jin, Sci. Rep. **3**, 2016 (2013).

[14] P. P. Kong, J. L. Zhang, S. J. Zhang, J. Zhu, Q. Q. Liu, R. C. Yu, Z. Fang, C. Q. Jin, W. G. Yang, X. H. Yu, J. L. Zhu, and Y. S. Zhao, J. Phys.: Condens. Matter **25**, 362204 (2013).

[15] K. Kirshenbaum, P. S. Syers, A. P. Hope, N. P. Butch, J. R. Jeffries, S. T. Weir, J. J. Hamlin, M. B. Maple, Y. K. Vohra, and J. Paglione, Phys. Rev. Lett. **111**, 087001 (2013).

[16] J. L. Zhang, S. J. Zhang, H. M. Weng, W. Zhang, L. X. Yang, Q. Q. Liu, S. M. Feng, X. C. Wang, R. C. Yu, L. Z. Cao, L. Wang, W. G. Yang, H. Z. Liu, W. Y. Zhao, S. C. Zhang, X. Dai, Z. Fang, and C. Q. Jin, Proc. Natl. Acad. Sci. USA **108**, 24 (2011).

[17] C. Zhang, L. L. Sun, Z. Y. Chen, X. J. Zhou, Q. Wu, W. Yi, J. Guo, X. L. Dong, and Z. X. Zhao, Phys. Rev. B **83**, 140504(R) (2011).

[18] M. Einaga, A. Ohmura, A. Nakayama, F. Ishikawa, Y. Yamada, and S. Nakano, Phys. Rev. B **83**, 092102 (2011).

[19] J. G. Zhao, H. Z. Liu, L. Ehm, Z. Q. Chen, S. Sinogeikin, Y. S. Zhao, and G. D. Gu, Inorg. Chem. **50**, 11291 (2011).

[20] Y. M. Ma, G. T. Liu, P. W. Zhu, H. Wang, X. Wang, Q. L. Cui, J. Liu, and Y. M. Ma, J. Phys.: Condens. Matter **24**, 475403 (2012).

[21] Z. H. Yu, L. Wang, Q. Y. Hu, J. G. Zhao, S. Yan, K. Yang, S. Sinogeikin, G. D. Gu, and H. K. Mao, Sci. Rep. **5**, 15939 (2015).

[22] H. Cheng, J. R. Zhang, Y. C. Li, G. Li, and X. D. Li, J. Appl. Phys. **121**, 225902 (2017).

[23] I. M. Lifshitz, Sov. Phys. JETP **11**, 1130 (1960).

[24] J. G. Checkelsky, Y. S. Hor, M. H. Liu, D. X. Qu, R. J. Cava, and N. P. Ong, Phys. Rev. Lett. **103**, 246601 (2009).

[25] Y. L. Chen, J. G. Analytis, J. H. Chu, Z. K. Liu, S. K. Mo, X. L. Qi, H. J. Zhang, D. H. Lu, X. Dai, Z. Fang, S. C. Zhang, I. R. Fisher, Z. Hussain, and Z. X. Shen, Science **325**, 178 (2009).

[26] D. X. Qu, Y. S. Hor, J. Xiong, R. J. Cava, and N. P. Ong, Science **329**, 821 (2010).

[27] S. K. Kushwaha, I. Pletikosic, T. Liang, A. Gyenis, S. H. Lapidus, Y. Tian, H. Zhao, K. S. Burch, J. J. Lin, W. D. Wang, H. W. Ji, A. V. Fedorov, A. Yazdani, N. P. Ong, T. Valla, and R. J. Cava, Nat. Commun. **7**, 11456 (2016).

[28] S. K. Kushwaha, Q. D. Gibson, J. Xiong, I. Pletikosic, A. P. Weber, A. V. Fedorov, N. P. Ong, T. Valla, and R. J. Cava, J. Appl. Phys. **115**, 143708 (2014).

[29] See Supplemental Material at http://link.aps.org/supplemental/10.1103/PhysRevB.97.174516 for additional experimental (single-crystal XRD, powder XRD, EDX, and Raman) information.

[30] C. Park, D. Popov, D. Ikuta, C. L. Lin, C. Kenney-Benson, E. Rod, A. Bommannavar, and G. Shen, Rev. Sci. Instrum. **86**, 072205 (2015).

[31] C. Prescher and V. B. Prakapenka, High Pressure Res. **35**, 223 (2015).

[32] B. A. Hunter, RIETICA—A visual Rietveld program, International Union of Crystallography Commission on Powder Diffraction Newsletter No. 20 (Summer 1998), http://www.rietica.org.

[33] H. K. Mao, J. Xu, and P. M. Bell, J. Geophys. Res. **91**, 4673 (1986).

[34] J. Xiong, Y. K. Luo, Y. H. Khoo, S. Jia, R. J. Cava, and N. P. Ong, Phys. Rev. B **86**, 045314 (2012).

[35] O. Pavlosiuk, D. Kaczorowski, and P. Wisniewski, Sci. Rep. **5**, 9158 (2015).

[36] H.-T. He, G. Wang, T. Zhang, I.-K. Sou, G. K. L. Wong, J.-N. Wang, H.-Z. Lu, S.-Q. Shen, and F.-C. Zhang, Phys. Rev. Lett. **106**, 166805 (2011).

[37] H. T. He, B. K. Li, H. C. Liu, X. Guo, Z. Y. Wang, M. H. Xie, and J. N. Wang, Appl. Phys. Lett. **100**, 032105 (2012).

[38] N. R. Werthamer, E. Helfand, and P. C. Hohenberg, Phys. Rev. **147**, 295 (1966).

[39] F. Birch, Phys. Rev. **71**, 809 (1947).

[40] V. Rajaji, P. S. Malavi, S. S. R. K. C. Yamijala, Y. A. Sorb, U. Dutta, S. N. Guin, B. Joseph, S. K. Pati, S. Karmakar, K. Biswas, and C. Narayana, Appl. Phys. Lett. **109**, 171903 (2016).

[41] V. Rajaji, U. Dutta, P. C. Sreeparvathy, S. C. Sarma, Y. A. Sorb, B. Joseph, S. Sahoo, S. C. Peter, V. Kanchana, and C. Narayana, Phys. Rev. B **97**, 085107 (2018).

[42] Y. H. Zhou, X. L. Chen, R. R. Zhang, J. F. Shao, X. F. Wang, C. An, Y. Zhou, C. Y. Park, W. Tong, L. Pi, Z. R. Yang, C. J. Zhang, and Y. H. Zhang, Phys. Rev. B **93**, 144514 (2016).